

NbN superconducting nanowire single photon detector with efficiency over 90% at 1550 nm wavelength operational at compact cryocooler temperature

W. J. Zhang, L. X. You*, H. Li, J. Huang, C. L. Lv, L. Zhang, X. Y. Liu, J. J. Wu, Z. Wang and X. M. Xie

State Key Lab of Functional Materials for Informatics,
Shanghai Institute of Microsystem and Information Technology (SIMIT), Chinese Academy of
Sciences (CAS), Shanghai, 200050, P. R. China
CAS Center for Excellence in Superconducting Electronics (CENSE)
865 Changning Rd., Shanghai, 200050, P. R. China.

[*lxyou@mail.sim.ac.cn](mailto:lxyou@mail.sim.ac.cn)

Abstract

The fast development of superconducting nanowire single photon detector (SNSPD) in the past decade has enabled many advances in quantum information technology. The best system detection efficiency (SDE) record at 1550 nm wavelength was 93% obtained from SNSPD made of amorphous WSi which usually operated at sub-kelvin temperatures. We first demonstrate SNSPD made of polycrystalline NbN with SDE of 90.2% for 1550 nm wavelength at 2.1K, accessible with a compact cryocooler. The SDE saturated to 92.1% when the temperature was lowered to 1.8K. The results lighten the practical and high performance SNSPD to quantum information and other high-end applications.

Main text

Single photon detector with high detection efficiency is the key enabling technology for quantum information and various applications, such as the test of the loophole-free Bell inequality violation¹, quantum teleportation², measurement-device-independent quantum key distribution³, and linear optical quantum computation⁴. Superconducting single photon detectors outperform the semiconducting counterparts in terms of not only detection efficiency, but also dark count rate, timing jitter and counting rate⁵. As for the telecommunication wavelength 1550 nm, two records of highest system detection efficiency (SDE) over 90% were reported for two types of detectors. One is transition edge sensor (TES) made of tungsten (W) with SDE of 95%⁶, the other is superconducting nanowire single photon detector (SNSPD) made of amorphous WSi with SDE of 93%⁷. However, due to the low superconducting transition temperature of the materials W and WSi, the requirement of sub-kelvin cryogenics turns to be an inescapable burden for practical applications. Many studies were focused on SNSPDs with different materials aiming to obtaining high SDE at higher operating temperatures⁸⁻¹¹, but unsuccessfully. Regarding to another important parameter, timing jitter, WSi SNSPD and W TES have the values of ~150 ps and 50-100 ns respectively, which limits the application requiring smaller timing jitter.

The SDE of SNSPD (η_{SDE}) can be expressed as the product of three contributions⁷: $\eta_{\text{SDE}} = \eta_{\text{oc}} \times \eta_{\text{abs}} \times \eta_{\text{int}}$, where η_{oc} is the optical coupling efficiency between the incident photons and active area, η_{abs} is the absorption efficiency of nanowires and η_{int} is the intrinsic detection

efficiency (IDE) which describe the pulse generation probability of the nanowire when a photon is absorbed. In order to achieve a high SDE, one has to maximize all the three parameters simultaneously. η_{oc} is mainly determined by the size of the active area of SNSPD when the optical alignment method is fixed. The impact factors of η_{abs} includes the geometric and optical parameters of the nanowire (thickness, width, filling ratio, refractive index) and the optical absorption enhancement structures (cavity). η_{int} is mainly determined by the superconductivity of the nanowire. However, the factors are complicated¹²⁻¹⁴. On one hand, the geometric parameters such as width, thickness of the nanowire play important roles. On the other hand, the operation parameters (bias current, operation temperature) may control the η_{int} directly. Besides, the uniformity of the nanowire (thickness variation, physical constrictions) handicaps η_{int} since it will suppress the maximum bias current. The above analysis indicates that η_{abs} and η_{int} are not independent, which are both related to the thickness and width of the nanowire. The correlation between η_{abs} and η_{int} makes the improvement of SDE complicated. Indeed, it is relatively simple for WSi SNSPD to reach high SDE since η_{int} can easily reach 100% with a wide range of nanowire thickness and width due to the lower pair-breaking energy of WSi. In the case of NbN SNSPD, it turns to be challenging since pair-breaking energy of NbN is nearly doubled and the room for tuning those parameters is very limited.

SNSPD made of NbN is a promising choice for practical application due to its high critical temperature, which gave the possibility of using the compact cryocooler for operation. Unfortunately, the highest SDE reported for the NbN SNSPD are less than 80% for 1550 nm wavelength¹⁵⁻¹⁷. Suspicion exists whether NbN is a candidate material for fabricating SNSPD with SDE over 90%.

In this manuscript, we answered the suspicion by demonstrating NbN SNSPD with SDE over 90% at 1550 nm wavelength. We introduced a DBR mirror on the Si substrate, with a measured reflectance of over 99.9% and a calculated absorption of the nanowire over 99%. The excellent front-side single-mode lens fiber coupling is guaranteed by a large sensitive area (over $\Phi 15 \mu\text{m}$). By tuning the film thickness, we were able to maximize the η_{abs} and η_{int} simultaneously. Measured with a dilution refrigerator, the saturated SDE reaches 92.1% when the temperature is lower than 1.8K. At 2.1K, the measured SDE is 90.2% at the dark count rate of 10 Hz, which is further verified by cooling SNSPD using a compacted Gifford-McMahon (G-M) cryocooler. Besides, due to the high switching current of NbN SNSPD, a timing jitter of 79 ps was obtained.

Results

Device design and structure. The design of SNSPDs at 1550 nm was based on the principle of integrating a DBR mirror to enhance the absorption of the nanowires. As shown in Fig.1 (a), the DBR was comprised fifteen-periodic $\text{SiO}_2/\text{Ta}_2\text{O}_5$ bilayers. The periodic bilayers were alternately deposited on a 400- μm -thick Si wafer using ion beam sputtering. Their thicknesses were fabricated to be a quarter of the 1550 nm wavelength, i.e., 265 nm for the SiO_2 layer ($n_{\text{SiO}_2}=1.46$) and 180 nm for the Ta_2O_5 layer ($n_{\text{Ta}_2\text{O}_5}=2.15$). The root-mean-square roughness of both the DBR substrate and the deposited NbN thin film on DBR was less than 0.3 nm (see Supplementary Fig.1). The measured reflectivity of the DBR substrate was greater than 99.9% at 1550 nm (see Supplementary Fig.2).

The nanowire linewidth was empirically designed to be 75 nm to enhance its η_{int} . With the linewidth fixed, numerical simulations with variable parameters, like the filling factors, thickness and configuration of cavity, were systematically investigated before the fabrications (see Supplementary Fig.3). The simulations indicated that a maximum absorption efficiency of over 99% can be realized with an NbN thickness of ~ 7 nm, with filling factor of ~ 0.5 , when integrated in a half-cavity (DBR/NbN/Air).

To experimentally validate the simulations, we prepared devices with various filling factors (0.58–0.33), and different film thicknesses (6.5–8.0 nm), covering two types of active areas ($\Phi 15$ and $18 \mu\text{m}$). The scanning electron microscopy (SEM) images of the nanowire with a nominal 75-nm width and 140-nm pitch is shown in Fig. 1(b), demonstrating a good controllability of the fabrication process. Figure 1(c) shows the TEM image of the DBR mirror. The measured thicknesses of deposited bilayers were found with ± 4 nm variation from the design values. Figure 1(d) shows a close-up TEM image of a cross-section of a nominal 7-nm-thick, 75-nm-wide nanowire, which has a slightly trapezoid shape due to the side-etching. The TEM image gave an estimated thickness of ~ 8 nm, which includes an oxidized layer (1–2 nm thick) on the top¹⁸.

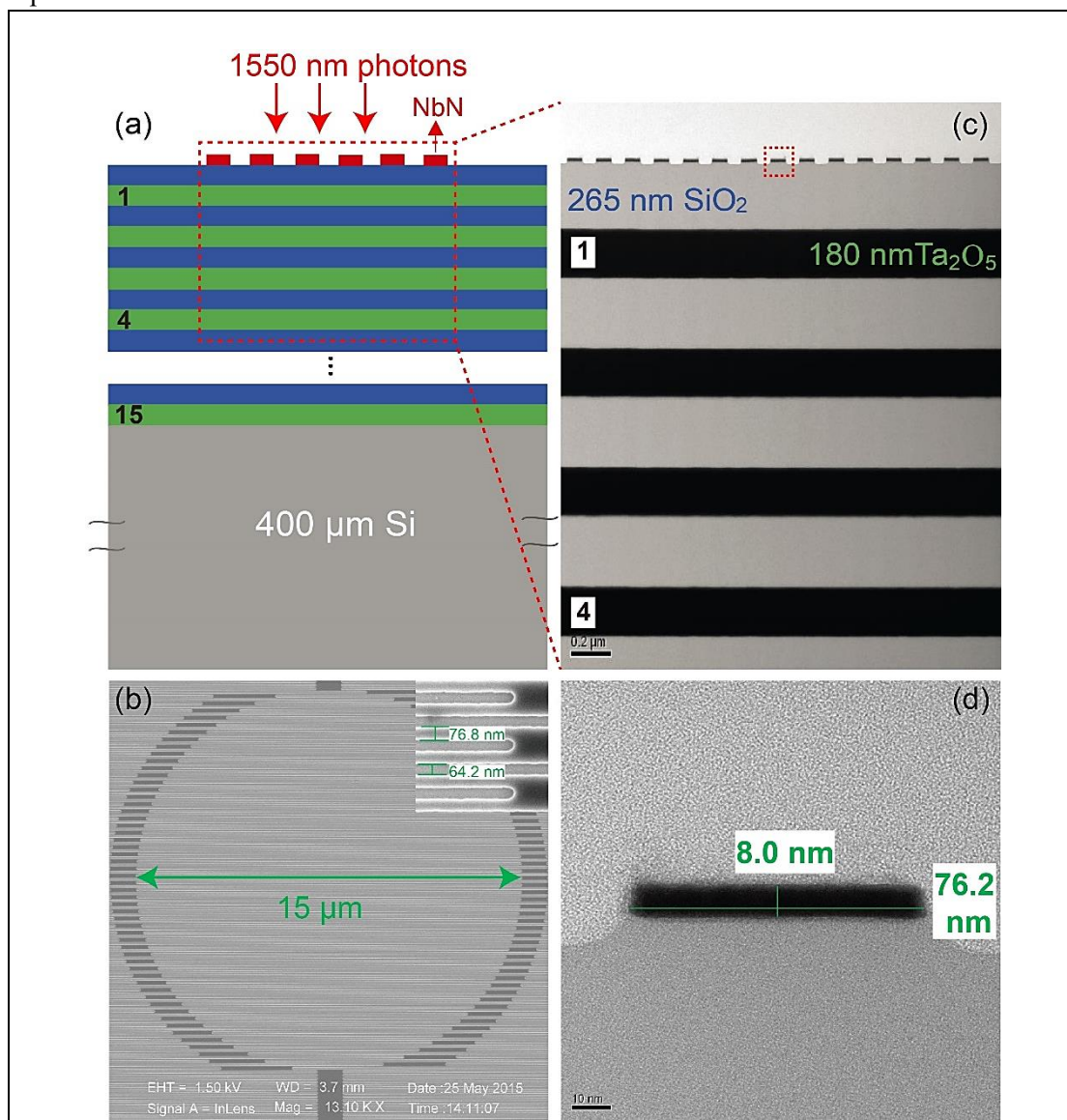


Fig.1. (Color online) (a) Schematic of a 7-nm-thick NbN SNSPD fabricated on a DBR/Si substrate. The DBR substrate comprised 15-periodic Ta₂O₅/SiO₂ bilayers deposited on a silicon wafer. (b) SEM image of nanowires. The diameter of the active area was 15 μm. The insert shows a zoom-in image of nanowires, with a nominal 77-nm width and 64-nm spacing. (c) TEM image of a cross section of nanowires on the DBR mirror. The thicknesses of the SiO₂ and Ta₂O₅ layer were about 265 and 180 nm, respectively. (d) Zoom-in TEM image of the cross section of a single nanowire, with a measured thickness of ~8.0 nm and width of ~76 nm. Due to an existing oxidization layer about 1-2 nm on the top, the effective NbN thickness of the nanowire was roughly estimated to be 7 nm.

Device Characterization. We characterized different SNSPDs with four film thicknesses (6.5, 7.0, 7.5 and 8.0 nm) fabricated in the same process run (see Supplementary Table 1). The corresponding T_{cs} are 7.8-8.6K with a monotonic increase with the film thickness (see Supplementary Fig.4). The detectors were screened by choosing those with the highest switching current for same geometrical parameters. Selected devices were then optically aligned to lens-single-mode fibers and mounted in a cryogen-free dilution refrigerator (CDR) which has a wide temperature range down to 16mK.

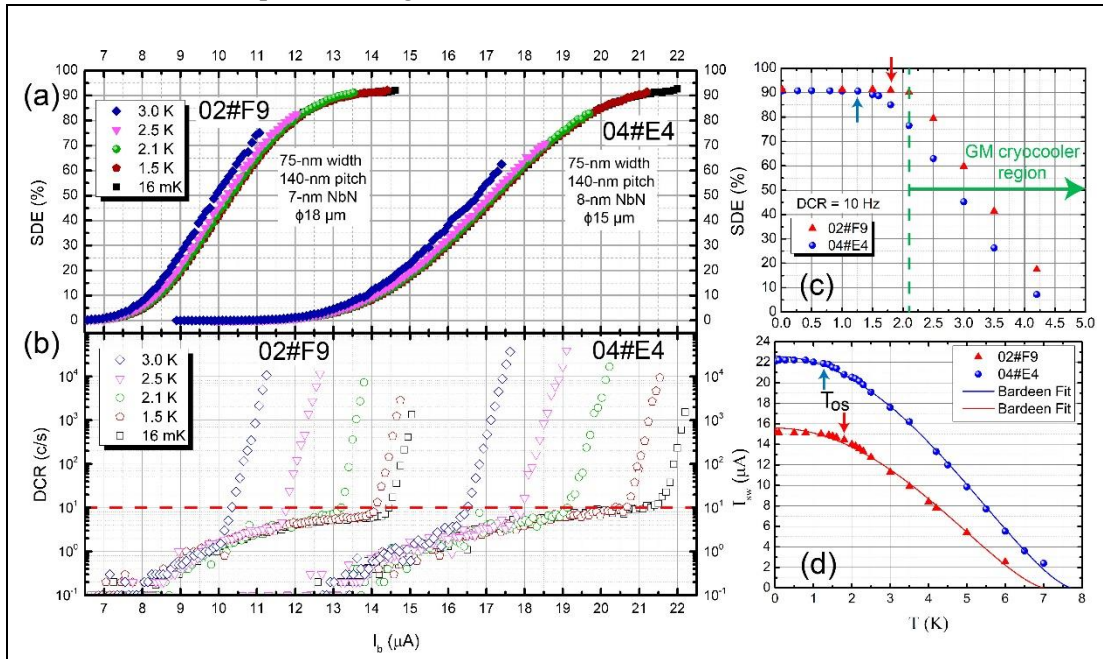


Fig.2. (Color online) (a) & (b) show the SDEs and DCRs as functions of the bias current I_b for the 7 and 8-nm-thick, 75-nm-wide, 140-nm-pitch SNSPDs, measured from 3K to 16mK. The filled and open symbols represent the SDE and DCR, respectively. As the temperature decrease, a clear saturation plateau emerged. The thinner NbN film was, a more saturated plateau can be observed. The maximal SDE of device 02#F9 and 04#E4 were 92.1% and 91.7%, respectively, operating at a DCR of 10 Hz. (c) Temperature dependence of SDEs for device of 02#F9, and 04#E4, when the DCR was set to 10 Hz. For 02#F9, the SDE of 90.2% can be obtained at temperature of 2.1K (indicated with green-dashed line), which also the base temperature for a GM cryocooler. The arrows implied the onset temperature (T_{os}) where the SDE nearly saturated as temperature decreased. (d) The switching current I_{sw} as a function

of temperature for the device 02#F9 and 04#E4.

Figure 2(a) and (b) show the SDEs for 1550 nm wavelength and DCRs as functions of the bias current I_b for two devices 02#F9 (7-nm-thick) and 04#E4 (8-nm-thick) at various temperatures. For clarity, five curves at five temperatures (3.0, 2.5, 2.1, 1.5K, and 16mK) were displayed. In the DCR measurement, the optical fiber port at room temperature was shielded to eliminate any stray light from the environment. By decreasing the operation temperature, the SDE increased and a saturation plateau appeared. When the temperature was lower than 3K, all the SDE(I_b) curves nearly overlapped at the same bias current. At the temperature of 1.5K and lower, we observed the highest SDE value of 92.1% for device 02#F9 at a DCR of 10 Hz and the saturation plateau indicating that the η_{int} reached $\sim 100\%$. When the temperature increased to 2.1K (the lowest temperature a commercial compacted G-M cryocooler may reach), the SDE of 90.2% can be obtained with a DCR of 10 Hz. For a 8 nm-thick NbN SNSPD (04#E4), it has a larger switching current (I_{sw}) of 22.5 μA compared to device 02#F9 with I_{sw} of 15.2 μA , and the highest SDE of 91.7% was measured at the DCR of 10 Hz at 16 mK. However, the SDE was decreased to 76.5% at 2.1K due to the weak saturation of SDE. To further verify high SDE over 90% at 2.1K, the SDE of device 02#F9 cooled with a G-M cryocooler (base temperature of 2.13K) was further examined using a G-M cryocooler (2.13K), which gave the value of 90.1% at DCR of 10 Hz (see Supplementary Fig.6). To the best of our knowledge, this is the first report for NbN SNSPD with SDE over 90%. More importantly, it was realized using the G-M cryocooler ($\sim 2.1\text{K}$), which provides a practical and affordable solution of single photon detection for quantum information.

The DCR increased monotonously with I_b at all temperatures. Two different regions can be clearly distinguished, which are background blackbody-radiation dominated DCR (low bias zone) and intrinsic vortex-related DCR (high bias zone). The intrinsic DCR logarithmically increased with I_b , which shifted to the high bias current with increase/decrease of I_{sw} /temperature. Its onset I_b depends on the temperature. For example, at the lowest temperature of 16mK for device 02#F9 (04#E4), the onset I_b was suppressed to $0.95(0.97)I_{\text{sw}}$, while it was $0.89(0.92)I_{\text{sw}}$ at 3K. On the other hand, the background DCR curves followed the same curve but the highest background DCR slightly increased due to the increase/decrease of I_{sw} /temperature. The same background DCR value at the bias current can be explained by the consistent SDE at the same bias current and stable background blackbody radiation.

Figure 2(c) shows temperature dependence of SDEs for device of 02#F9 and 04#E4 at DCR of 10 Hz. The green-dashed line indicates the lowest temperature that a commercial G-M cryocooler may reach directly (for example, SHI RDK-101D from Sumitomo Inc.^{16, 19}). For both devices, the SDE increased with a decrease of the temperature, and saturated at low temperatures. The onset temperature (T_{os}) where SDE reaches its saturation as temperature decreases was indicated with the arrow in the figure. The T_{os} of 02#F9 and 04#E4 were 1.8K and 1.3K, respectively. Due to the wide saturated plateau, the SDE(T) of 02#F9 demonstrates a slow decrease as the temperature increased, in contrast to the one of 04#E4. The different saturation behavior was due to the film thickness difference, which will be discussed later.

Figure 2(d) shows the temperature dependence of I_{sw} s for device of 02#F9 and 04#E4. The I_{sw}

had a measurement error about $\pm 0.05 \mu\text{A}$. When the temperature was lower than T_{os} , the I_{sw} gradually reached a maximum. The I_{sw} s at T_{os} were equaled to 14.5 and 21.9 μA , respectively. A fitting based the Bardeen model²⁰ simplified as $I_{\text{cd}} = \alpha \cdot (1 - (T/T_c)^2)^{3/2}$ was applied to the measured I_{sw} s and plotted as the dashed lines, where α and T_c were the variable parameters. The fitting is consistent with the measured data well except with a slight deviation at the low temperature region ($T < 1\text{K}$). Since the existence of possible constrictions in the nanowire which may limit the experimental maximal I_{sw} , it was expected that the measured I_{sw} could be smaller than the calculated depairing current I_{cd} .

To experimentally study the performance of the optical design, we measured the wavelength dependence of the maximum SDE_{\parallel} and SDE_{\perp} when the polarization of the photons is parallel and vertical to the direction of the nanowire. For comparison, the simulated absorption A is also given from 1200 to 1800 nm. As shown in Fig.3, the absorption A_{\parallel} showed a broad peak with a value of 99.5% (98.1%) for 7(8) nm thick nanowire at wavelength around 1550 nm. The measured SDE_{\parallel} s are roughly 7% lower than the calculated absorption while SDE_{\perp} s are $\sim 6\%$ higher than the corresponding calculated absorption. In other words, the measured polarization extinction ratio (PER, defined as $\text{SDE}_{\parallel}/\text{SDE}_{\perp}$) is lower than the calculated PER (defined as A_{\parallel}/A_{\perp}). For example, for 7(8)-nm-thick device, the experimental PER of 3.5(3.2) at 1550 nm was lower than the calculated one of 4.4(4.6). The deviation indicated that the practical device was different from the design in geometry and/or material optical parameters. Further optimization of the fabrication process will be helpful to further improve the consistence and the SDE. Besides, an extra ARC upon the nanowire may suppress the PER by twice or even more if it is necessary (see Supplementary Tab. 1). On the other hand, the SDE drops faster than the simulated value when the wavelengths were larger than 1600 nm, which can be explained by a non-unity η_{int} due to the smaller photon energy (see Supplementary Fig.8).

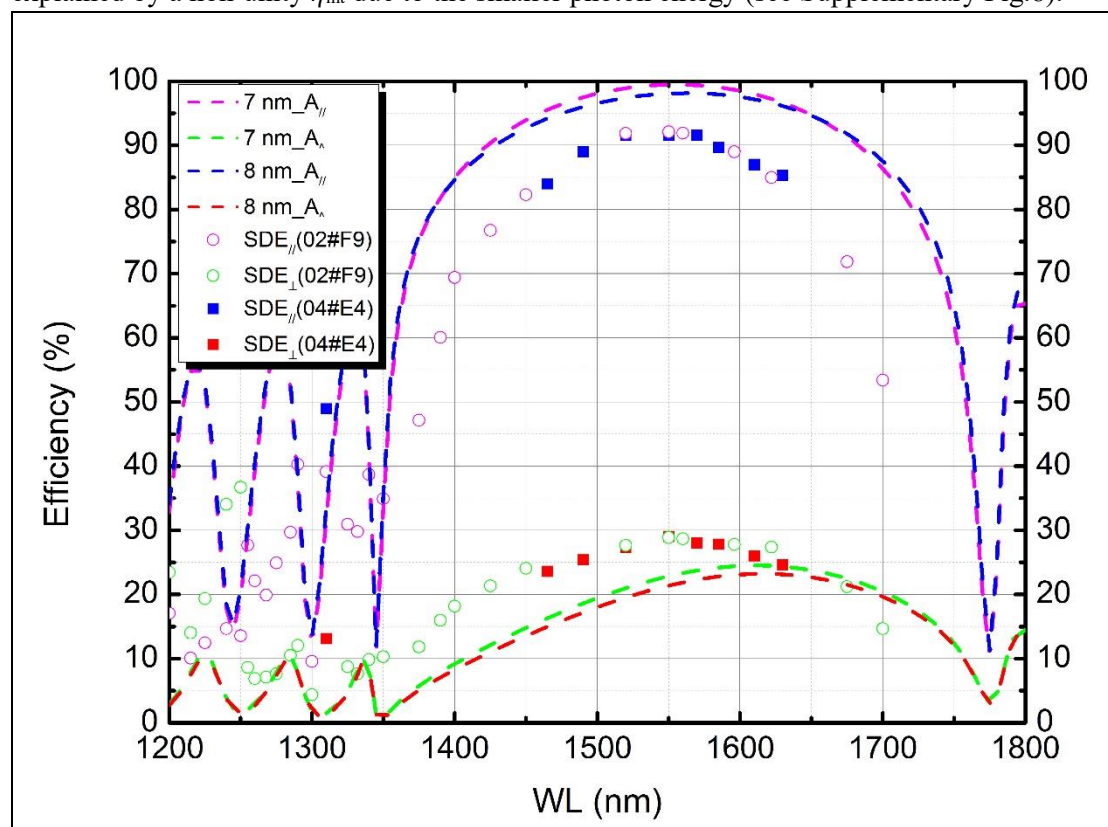


Fig.3. (Color online) Wavelength dependence of the measured SDEs for the device 02#F9 (open circle) and 04#E4 (solid square) in a range from 1200 to 1800 nm. The SDEs were recorded when the bias current was 14.0 and 21.0 μA , respectively, with a DCR of 10 Hz. The dashed lines show the simulated parallel ($A_{//}$, magenta and blue) and perpendicular (A_{\perp} , green and red) polarized absorption as functions of wavelengths for 7 and 8 nm thick nanowires, both with a 75-nm width and 140-nm pitch.

The above results indicate that NbN SNSPD presented SDE of 90% at the dark count rate of 10 Hz at 2.1K. The other important parameter, timing jitter T_j , was also measured at 16mK and 2.1K. Figure 4 shows T_j of the SNSPDs (device 02#F9 and 04#E4), measured at a bias current of 14.5 and 21.5 μA (both at $0.95I_{\text{sw}}$), using a time-correlated single-photon counting (TCSPC) module (SPC-150, Becker & Hickl GmbH). A 1550-nm-wavelength pulsed laser with a 100 fs pulse width was used, and the input photon flux was attenuated to the single-photon level. For the devices 02#F9 and 04#E4, T_j defined by the full width at half maximum (FWHM) of the histogram were 70.2 and 40.0 ps at 16 mK and increased to 79.0 and 46.0 ps at 2.1 K, due to the reduction of I_b . It is worth to note that, the values of T_j measured at CDR were a few ps larger than the ones measured at G-M cryocooler at the same bias current, due to the long coaxial cable (about 4.5 m) applied in the cryogenic system. Even though, the measured T_j of NbN SNSPD is roughly 2 times smaller than T_j of WSi SNSPD due to the much larger of the switching current (3 times larger roughly). Figure 4(b) shows the bias current dependence of T_j , which implied that the signal-to-noise ratio played the key role in determining T_j . More parameters' comparison between the Nb(Ti)N, WSi, MoSi-SNSPDs and W-TES can be found in the Supplementary Tab.2, significant advances have been achieved by our NbN detectors.

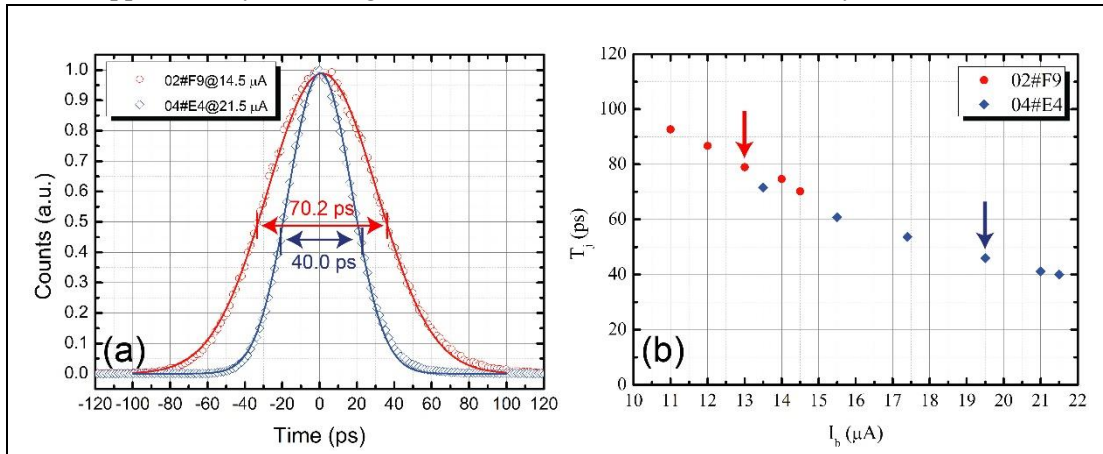


Fig.4. (Color online) (a) timing jitter (T_j) measurement of two devices measured at temperature of 16 mK. For device 02#F9 and 04#E4, the corresponding FWHM values of T_j are 70.2 and 40.0 ps, respectively, with a Gaussian fitting (see solid lines); (b) Bias current dependence of T_j . The T_j increased to 79.0 and 46.0 ps at 2.1K (indicated with arrows) due to the reduction of I_b to 13.0 and 19.5 μA for the devices 02#F9 and 04#E4, respectively.

Discussion

A few approaches are contributed to the remarkable improvement of the SDE. The first one is the DBR cavity design, which guarantee a near-unity reflectance at 1550 nm photons. The

second one is the front-side lens fiber alignment removes the reflection of the substrate in the backside fiber-coupled SNSPDs. Third, the use of lens fiber guarantees better optical coupling between the nanowire and the incident photons, due to a smaller beam size than the one of SM-28e fiber. The third approach is to maximize the optical absorption and IDE simultaneously by tuning the thickness with fixed nanowire linewidth. It seemed that the optimization reached with the nominal film thickness of 7 nm. The absorption reaches the maximum while IDE is also very close to unity even at 2.1K. For the film thickness of 8 nm, less saturated SDE behavior was observed at 2.1K, though the maximum SDE is 91.7% at 16mK. With the thinner film thickness of 6.5 nm, a more saturated SDE behavior was registered for SNSPD at 2.1K, however, the highest SDE is only 82%, which indicated a low optical absorption (see Supplementary Fig.7).

In conclusion, we successfully demonstrated that SDE of NbN SNSPD surpassed 90(92) % at DCR of 10 Hz at 2.1(1.8)K, due to the adoption of DBR mirror and the simultaneous maximization of the optical absorption and IDE. Besides, the NbN SNSPD featured a timing jitter of 79 ps. We believe there are some room for further improving SDE by optimizing the fabrication process, optical and superconducting properties of the film, going towards SDE of near unity and higher operation temperature.

Methods

Device preparation. A series of NbN films with various nominal thicknesses from 6.5 nm to 8 nm were deposited onto the 2 inch DBR wafers at room temperature. The deposition of NbN thin film were performed in a reactive direct-current magnetron sputtering system when the partial pressures of the Ar-N₂ gas mixture were 79% and 21%, respectively. The thickness of the film was controlled by the sputtering time and verified by the XRD analysis. Then, the NbN film was patterned into a meandered nanowire structure using electron beam lithography (EBL) with a positive-tone ZEP520A electron-beam resist and was reactively etched in CF₄ plasma. The width of nanowire was fabricated to ~75 nm with different pitch of 130, 140, 160, 180, 200, and 230 nm. Finally, a 50-Ω-matched coplanar waveguide was formed using ultraviolet lithography and reactive ion etching. The active areas of SNSPDs were designed with two sizes (Φ15 and Φ18 μm), which are much larger than the 6.8-μm mode field diameter of a lens fiber for 1550 nm. The lens fiber was designed with a focal distance~145 μm, ARC target wavelength at 1550 nm, and reflectance less than 1%. The fiber is aligned to the center of the active area using a microscope at room temperature, the alignment error is estimated to be ±3 μm. The devices with the lens fiber were packaged in a copper box.

Measurement setup. Figure 6 shows a schematic diagram of our measurement system incorporating a CDR. The fiber-coupled package was mounted on an Au-plated oxygen-free copper platform thermally connected to the mixing chamber of the CDR with a base temperature of 10 mK. The sample temperature was indicated by a RuO_x resistance thermometer located at the bottom of mixing chamber. The dilution unit is inside a fridge dewar mounted on a vibration-attenuated stage. The temperature was tuned using a Proportional-Integral-Derivative (PID) controller. The temperature stability were different on varied temperature regions: T ≤ 1K, ±0.001K; T ≤ 1.8K, ±0.04K; T ~ 2K, ±0.06K; T ≥ 2.3K, ±0.03K.

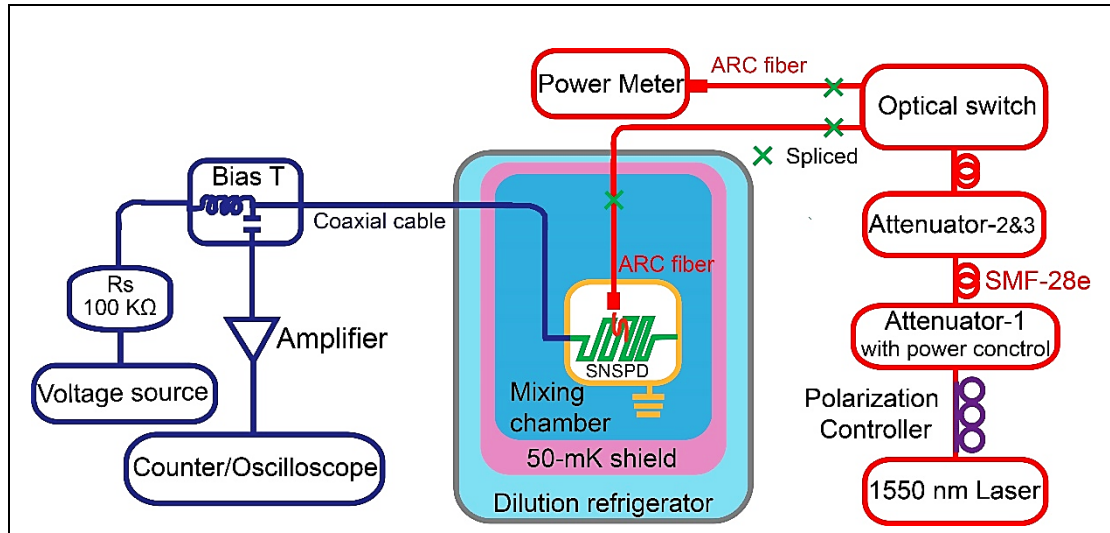


Fig.5. (Color online) Schematic diagram of an ultralow-temperature measurement system for the SNSPDs. The SNSPDs are mounted on the plate of the mixing chamber which can easily control the temperature from 16mK to 8K by the PID controller. Optical (represented by red lines) and electric (represented by blue lines) components are indicated in the figure.

A spliced single-mode (SM) optical fiber and a 50-Ω coaxial cable were connected from the top of the fridge to the SNSPD package. The coupling loss due to the fiber splicing was typically ~ 0.01 dB. In order to suppress the blackbody radiation of the fiber, the SM fiber was coiled in the mixing chamber with a diameter of about 30 mm. The optical loss due to the coils were carefully checked and found less than 0.07 dB at 1550 nm wavelength. Two tunable-wavelength continuous-wave (CW) laser diodes (Keysight 81970, 1465–1575 nm; Keysight 81940, 1520–1630 nm) and a supercontinuum white light laser (NKT photonics, EXB-3) were used as the photon sources. The input light was heavily attenuated by three cascaded attenuators so that the photon flux at the input connector of the cryostat was single-photon level. A polarization controller (Agilent N7786B) was inserted in front of the attenuator together with power controller to obtain the maximum SDE. Each time of tuning the polarization, the input power was carefully rechecked by switching the input photons to the power meter (Keysight 81624B) port. The split ratio of the MEMS optical switch was $1:1.002 \pm 0.002$, guaranteed a nearly identical input photon number to the power meter and the SNSPD. The power calibration was performed at a level of -38.930 ± 0.006 dBm, which was at the linear region of the power meter. Then a cascaded attenuation of -33 and -40 dB by using two attenuator was adopted to the input photons, and a final input power reached -111.930 dBm, corresponding to a photon flux of 5×10^4 photons/s. The linearity of the three attenuators were recalibrated by the power meter, which were found to be 0.999 ± 0.001 (see Supplementary Figure 5).

The device was current-biased through the dc arm of the bias tee. The response pulse of the detector was readout via the ac arm of the bias tee with a room-temperature amplifier (RF Bay Inc., LNA650) and photon counter (SRS Inc., SR400). The SDE was defined as $SDE = (PCR - DCR)/(5 \times 10^4)$, where PCR is the output pulse rate of the SNSPD.

The SDEs included all losses in the system and the overall relative errors of the SDE values

could be estimated to be 2.82%, resulting from the relative uncertainty of the power meter calibration (2.80%)²¹, the uncertainty of the splitting ratio (0.20%), uncertainty of the attenuation (0.33%), and uncertainty of the PCR (0.10%). The dominated uncertainty was from the light power calibration, which can be further reduced by using the Agilent calibration option C05²¹ or the correlated-photon-based method²².

References

1. Giustina M, *et al.* Significant-Loophole-Free Test of Bell's Theorem with Entangled Photons. *Physical Review Letters* **115**, 250401 (2015).
2. Sun Q, *et al.* Quantum teleportation with independent sources over an optical fibre network. Preprint at <http://arxiv.org/abs/1602.07081> (2016).
3. Tang YL, *et al.* Measurement-Device-Independent Quantum Key Distribution over 200 km. *Phys Rev Lett* **113**, 190501 (2014).
4. Knill E, Laflamme R, Milburn GJ. A scheme for efficient quantum computation with linear optics. *Nature* **409**, 46-52 (2001).
5. Hadfield RH, Johansson G. *Superconducting Devices in Quantum Optics*. Springer (2016).
6. Lita AE, Miller AJ, Nam SW. Counting near-infrared single-photons with 95% efficiency. *Optics express* **16**, 3032-3040 (2008).
7. Marsili F, *et al.* Detecting single infrared photons with 93% system efficiency. *Nat Photon* **7**, 210-214 (2013).
8. Verma VB, *et al.* High-efficiency superconducting nanowire single-photon detectors fabricated from MoSi thin-films. *Optics express* **23**, 33792-33801 (2015).
9. Dorenbos SN, *et al.* Low gap superconducting single photon detectors for infrared sensitivity. *Applied Physics Letters* **98**, 251102 (2011).
10. Engel A, *et al.* Tantalum nitride superconducting single-photon detectors with low cut-off energy. *Applied Physics Letters* **100**, 062601 (2012).
11. Yu PK, *et al.* Superconducting single-photon detector made of MoSi film. *Superconductor Science and Technology* **27**, 095012 (2014).
12. Semenov A, Engel A, Hubers HW, Il'in K, Siegel M. Spectral cut-off in the efficiency of the resistive state formation caused by absorption of a single-photon in current-carrying superconducting nano-strips. *The European Physical Journal B* **47**, 495-501 (2005).
13. Marsili F, *et al.* Single-photon detectors based on ultranarrow superconducting nanowires. *Nano letters* **11**, 2048-2053 (2011).

14. Renema JJ, *et al.* Experimental Test of Theories of the Detection Mechanism in a Nanowire Superconducting Single Photon Detector. *Physical Review Letters* **112**, 117604 (2014).
15. Rosenberg D, Kerman AJ, Molnar RJ, Dauler EA. High-speed and high-efficiency superconducting nanowire single photon detector array. *Opt Express* **21**, 1440 (2013).
16. Yamashita T, Miki S, Terai H, Wang Z. Low-filling-factor superconducting single photon detector with high system detection efficiency. *Opt Express* **21**, 27177-27184 (2013).
17. Chen S, *et al.* Dark counts of superconducting nanowire single-photon detector under illumination. *Opt Express* **23**, 10786-10793 (2015).
18. Semenov A, *et al.* Optical and transport properties of ultrathin NbN films and nanostructures. *Physical Review B* **80**, 054510 (2009).
19. *RDK-101D 4K Cryocooler Series*, <<http://www.shicryogenics.com/products/4k-cryocoolers/rdk-101d-4k-cryocooler-series/>> (2016).
20. Bardeen J. Critical Fields and Currents in Superconductors. *Reviews of Modern Physics* **34**, 667-681 (1962).
21. *See the manual of Agilent 81624B. The total uncertainty of Calibration option C01/C02 was about 2.8%, while the PTB (Technische Bundesanstalt, the German national metrology institute) traceable calibration option C05 could reduce the uncertainty down to 0.8%. <<http://literature.agilent.com/litweb/pdf/5988-7520EN.pdf>>* (2016).
22. Polyakov SV, Migdall AL. High accuracy verification of a correlated-photon-based method for determining photon-counting detection efficiency. *Optics express* **15**, 1390-1407 (2007).

Acknowledgments

The authors would like to thank M. Wang, ZJ. Li and B. Gao from SIMIT for technical support of the ultra-low temperature measurement. This work was funded by the National Natural Science Foundation of China (91121022, 61401441, & 61401443), Strategic Priority Research Program (B) of the Chinese Academy of Sciences (XDB04010200) and the Science and Technology Commission of Shanghai Municipality under Grant 16JC1400402.

Author contributions

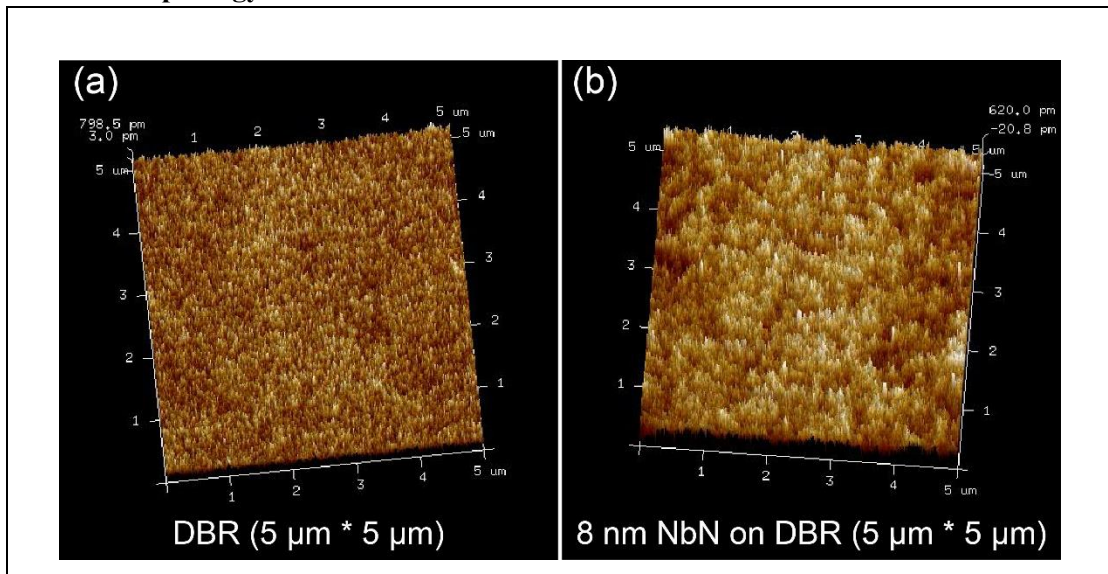
W.J.Z. designed and fabricated the devices. W.J.Z. and L.X.Y. wrote the paper. L.X.Y. organized the research. H.L. performed numerical simulations. W.J.Z. and J.H. performed the measurements. C.L.L. helped to perform the ultra-low temperature measurement with constructive discussions. L.Z. and J.H. provided the NbN films. X.Y.L., J.J.W., Z.W., X.M.X. and M.H.J. provided helpful discussions. All authors reviewed the manuscript.

Additional information

Competing financial interests: The authors declare no competing financial interests.

Supplementary Information

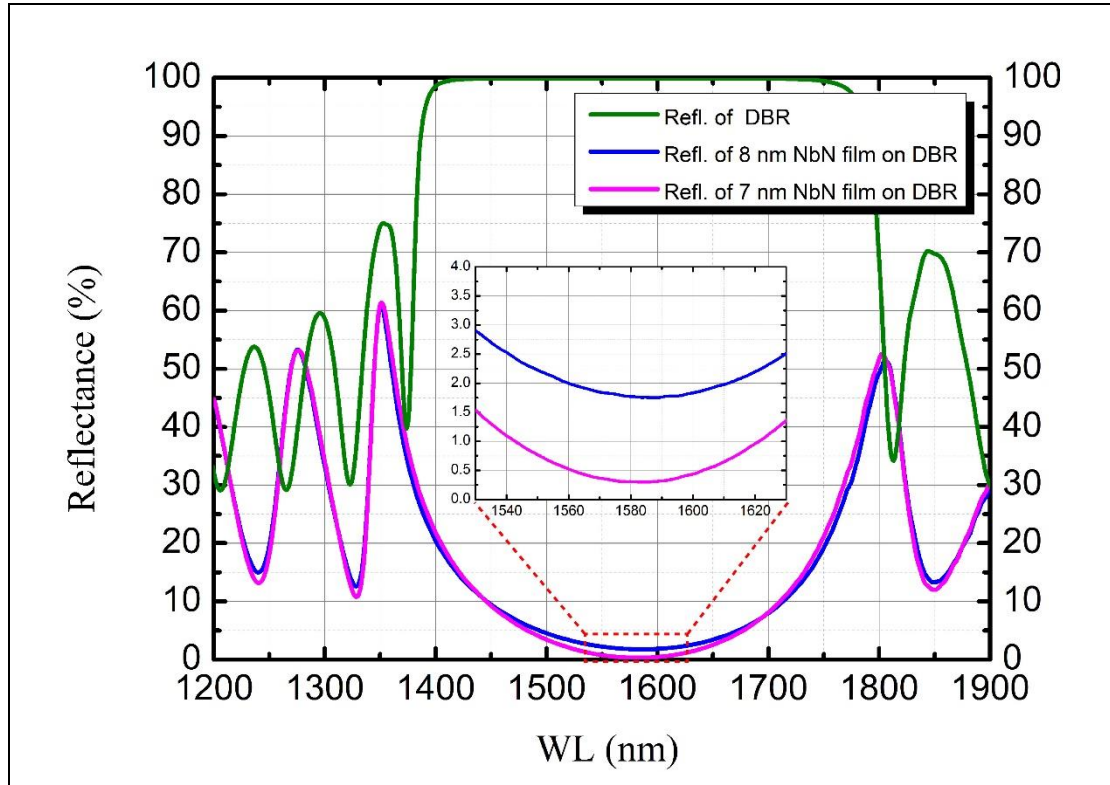
Surface morphology of the NbN films



Supplementary Figure 1 (Color online) Atomic force microscope (AFM) images of the DBR substrate and the 8.0-nm NbN film deposited on DBR. The roughness of the DBR substrate and NbN film were about 0.2 and 0.3 nm.

In order to characterize the uniformity of the film thickness, high resolution atomic force microscopy (AFM) measurements were performed. The surface morphology of the DBR substrate and an 8.0-nm NbN thin films deposited on DBR were presented in Supplementary Fig. 1. From the AFM image, a RMS (root mean square) surface roughness of 0.2 and 0.3 nm were determined. The roughness of NbN film was a little larger than the one of DBR due to the lattice mismatch. From the measurements we found that thickness variations of the NbN film less than a few percent.

Measurement of reflectance of NbN film on DBR

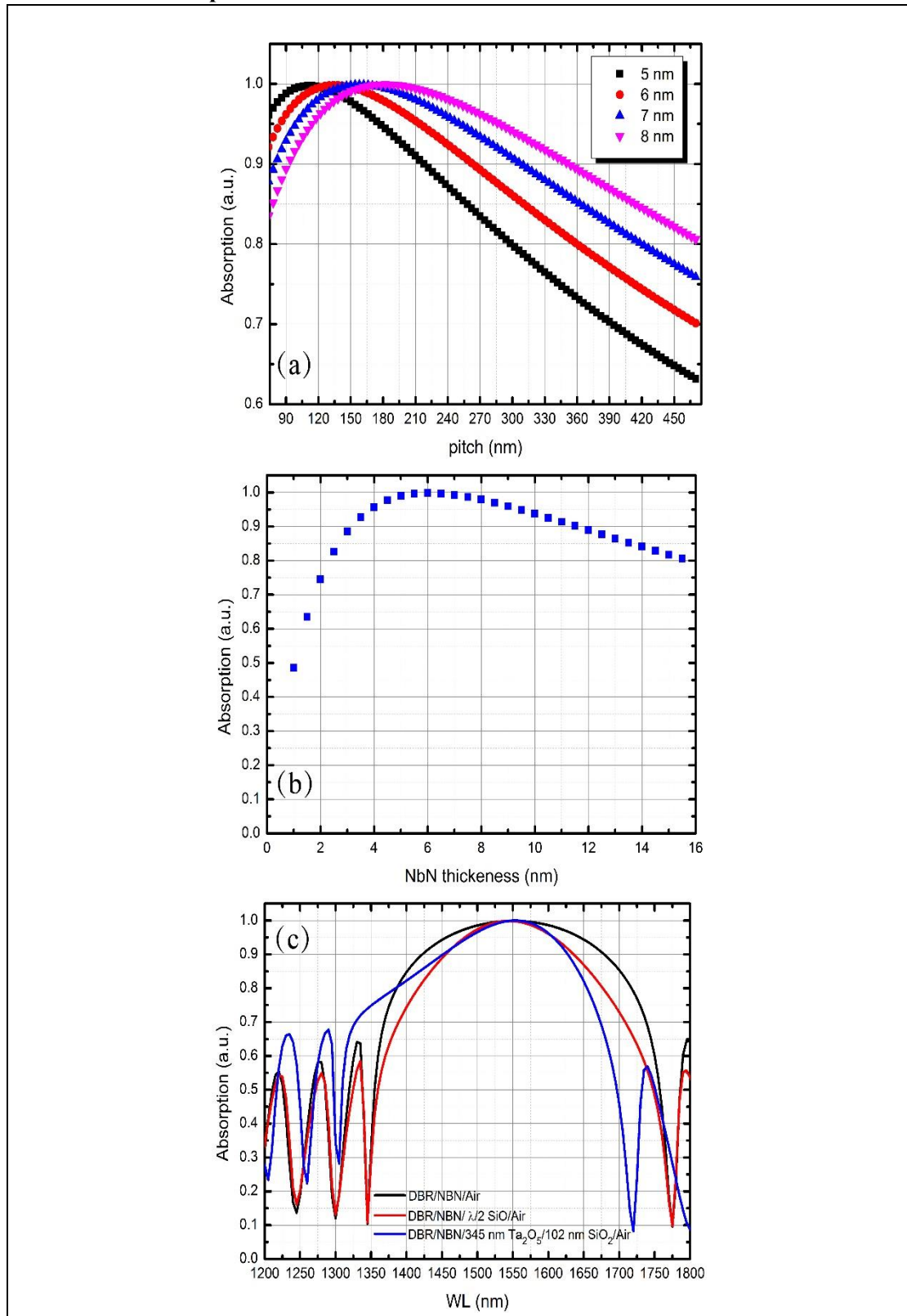


Supplementary Figure 2. (Color online) Wavelength dependence of the reflectance of DBR wafer (R_{DBR}) and NbN films deposited on DBR wafer (R_{NbN}) with thickness of 7 and 8 nm, measured at room temperature by a spectrophotometer. At 1550 nm wavelength, the R_{DBR} and R_{NbN} for 7(8) nm were 99.9% and 0.77(2.24)%, respectively. The insert shows a zoom-in region around the minima of the R_{NbN} for 7(8) nm.

Since the absorption A can be expressed as $A = 1 - Tr - R$ and the transmission Tr is negligible ($\sim 0.1\%$) for the high reflectance mirror, the reflectance R can be directly measured by a spectrophotometer, then A can be deduced as $A \sim 1 - R$. Figure 4 shows the measured reflectance as a function of wavelengths from 1200 to 1900 nm, for the NbN thin films deposited on DBR mirror with the thickness of 7(8) nm. The reflectance minima appears around 1570-1600 nm, implied high absorption of NbN film in these wavelengths.

The measured reflectance data shows that near-unity absorption in NbN film can be obtained when the film thickness on the DBR mirror is about 7 nm. As the thickness increase, the reflectance increases. However, it should be noted that, the absorption of thin film (A_{film}) could be different from the absorption of nanowire or device (A_{device}), and the A_{film} defines the upper bound for A_{device} .

Simulation of absorption for devices



Supplementary Figure 3. (Color online) (a) Simulated absorptions of devices as a function of the pitch with a fixed width (75 nm) and thickness (5, 6, 7, 8 nm). (b) Simulated absorptions of devices as a function of the NbN thickness, with a fixed width (75 nm) and pitch (140 nm). (c) Wavelength dependence of absorptions for the half (black line) and full-

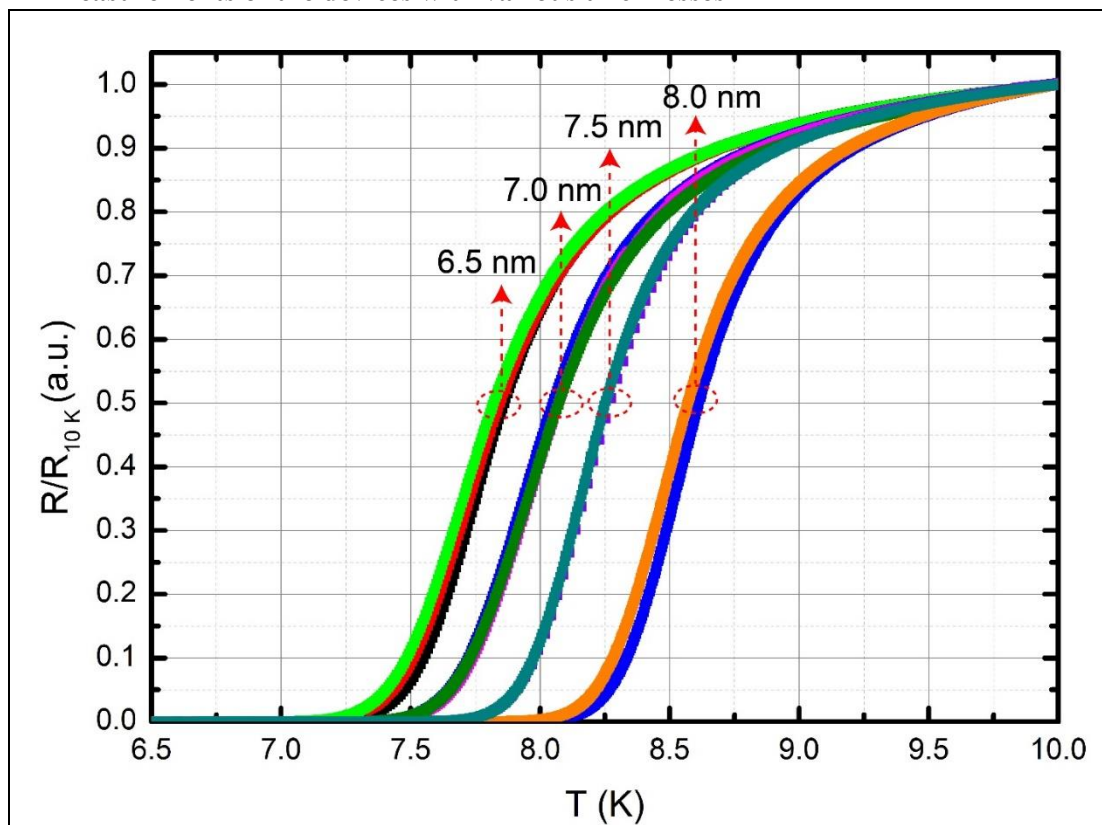
cavity (red, blue and green lines) devices, with a fixed width (75 nm) and pitch (140 nm). For the full-cavity designs, their front anti-reflection coating (ARC) were tuned with varied dielectric materials. The introduced ARC to the half cavity design resulted in narrowing the bandwidth.

In order to optimize the A_{device} , numerical simulations were performed by the rigorous coupled-wave analysis method. The parameters in the simulation, i.e., the refractive index of NbN, $n_{\text{NbN}} = 6.50 + 5.83i$, at 1550 nm was obtained using a spectroscopic ellipsometer, and the refractive index and thickness of the Si substrate were $n_{\text{Si}} = 3.46$, and $L = 400 \mu\text{m}$, respectively.

Supplementary Fig.3 (a) shows the A_{device} as a function of pitch with a fixed 75-nm width for the case at different thicknesses (5.0-8.0 nm). In the case of thickness at 7.0 nm, maxima over 99% appeared at the pitch ranging from 130 to 190 nm. As the thickness increases, the position of the maxima shifted to a large pitch, i.e., a larger spacing is necessary for thicker film. As shown in Supplementary Fig.3 (b), the A_{device} with fixed width and pitch (75 and 140 nm) first increased then fell gradually as the NbN thickness increased. A_{device} reached a maxima over 0.99 at 5.5-7.0 nm.

Supplementary Fig.3 (c) shows the influence of the anti-reflection coating (ARC) on the half-cavity (DBR/NbN/Air) design. The designs of ARC were tuned with several types of materials, such as SiO (the SiO refractive index $n_{\text{SiO}} = 1.89$), SiO₂ and Ta₂O₅. It can be found that the ARC coatings (SiO and SiO₂/Ta₂O₅ bilayer) did not significantly change the absorption around the target wavelengths but resulted in a reduction of bandwidth. Therefore, for a simplified fabrication process, the half cavity design can provide a high enough absorption over 0.995.

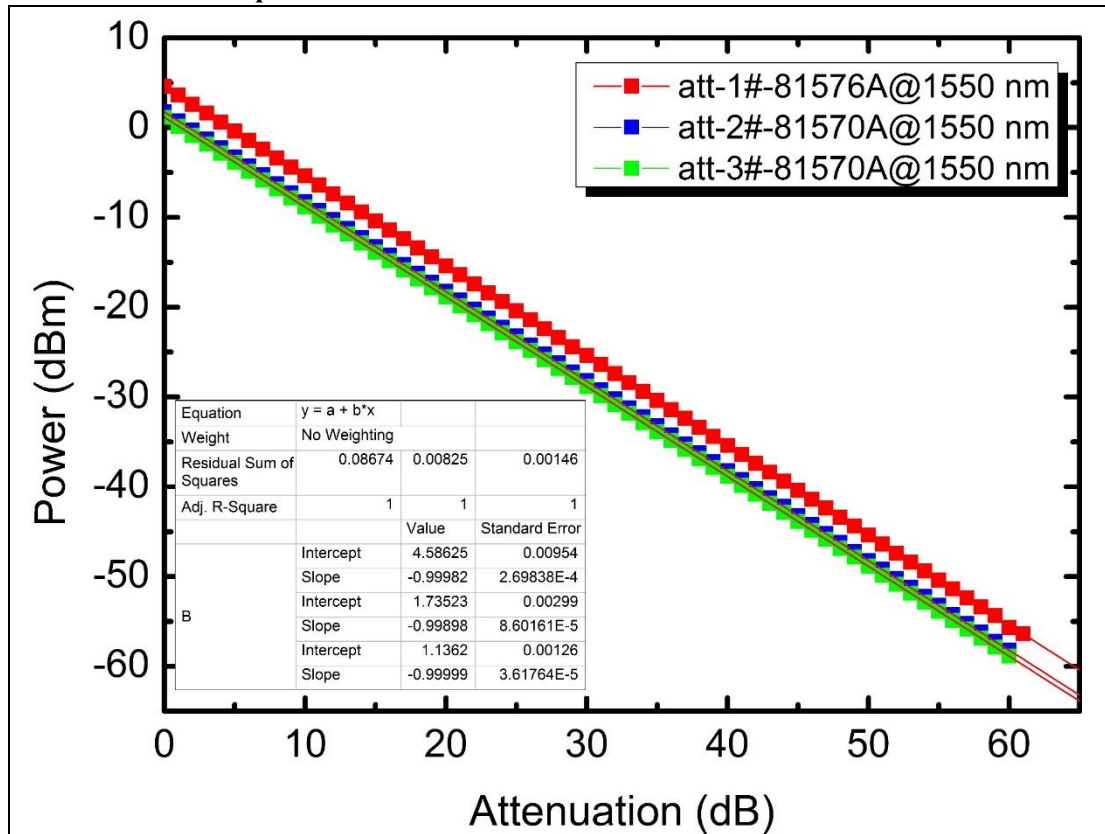
RT measurements of the devices with various thicknesses



Supplementary Figure 4. (Color online) Normalized Resistance of 10 devices as functions of temperature with NbN thickness of 6.5, 7.0, 7.5 and 8.0 nm. The resistance R was normalized by divided the resistance value at 10K (R_{10K}). The T_{cs} (defined by $0.5R/R_{10K}$) of 6.5, 7.0, 7.5 and 8 nm devices are 7.85, 8.07, 8.26 and 8.59K, respectively, with an error about $\pm 0.05K$.

Supplementary Figure 4 shows the RT measurements for 10 devices with different nominal thickness from 6.5 to 8.0 nm. The curves were normalized by its resistance value at 10K (R_{10K}). The T_c of thin film was determined by the criterion of $0.5R/R_{10K}$. The deposited rate of NbN film was about 0.8 nm/s and the thickness was controlled by the deposited time. Since these NbN film were fabricated in the same run. Clear separation of the RT curves for each thickness was obtained, indicated a good control of deposited NbN thickness.

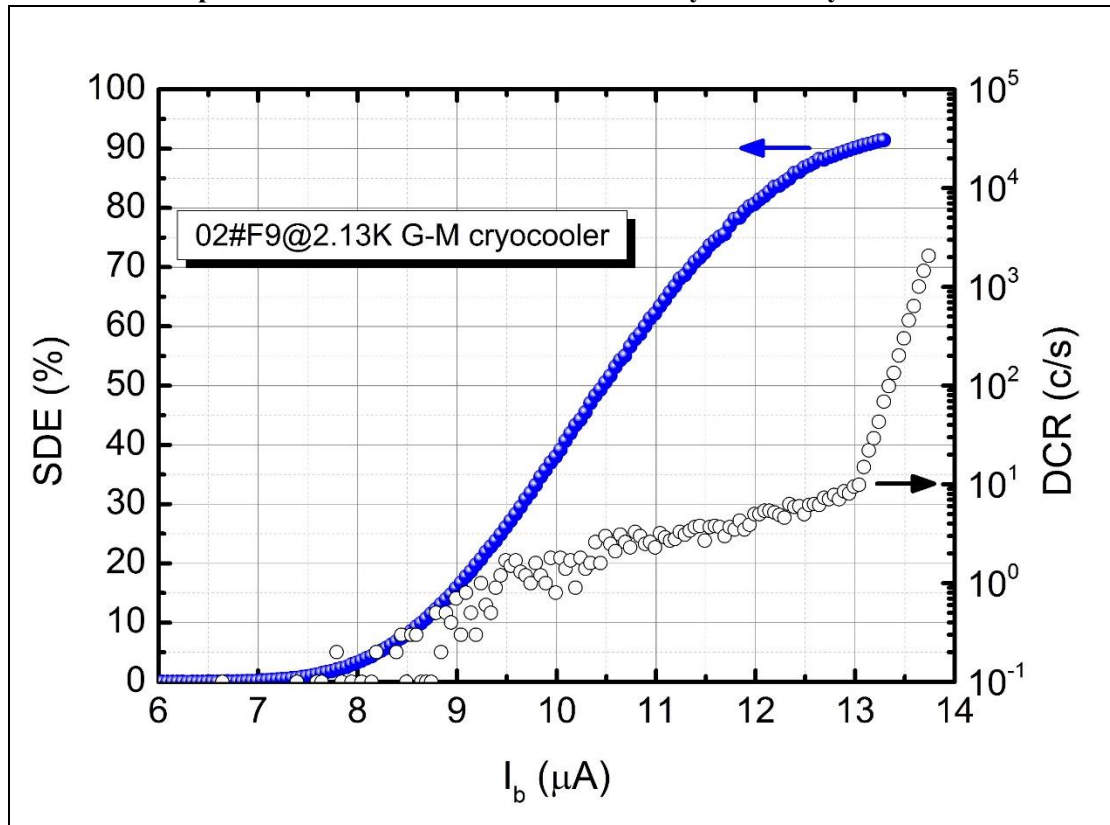
Calibration of the optical attenuators



Supplementary Figure 5. (Color online) Measurement of the individual attenuator linearity with varying input power at the wavelength of 1550 nm. Three independent attenuators are able to supply up to 180 dB of optical power reduction. All the output power were measured by the same power meter (Keysight 81624B). All the attenuators showed good linearity closed to unity, independent on input optical power.

Three attenuators (one is 81576A, two are 81570A) were calibrated separately to confirm the expected linearity particularly at high attenuation values. Supplementary Fig. 5 showed the measured transmitted power as a function of nominal attenuation. The attenuation was measured at input power levels of 1~5 dBm, which emitted from the tunable laser source (Keysight 81940A) employed in the SNSPD characterizations. The linear fitting revealed that the linearity of the attenuators was at the level of 0.999 ± 0.001 , ensured a precise attenuation.

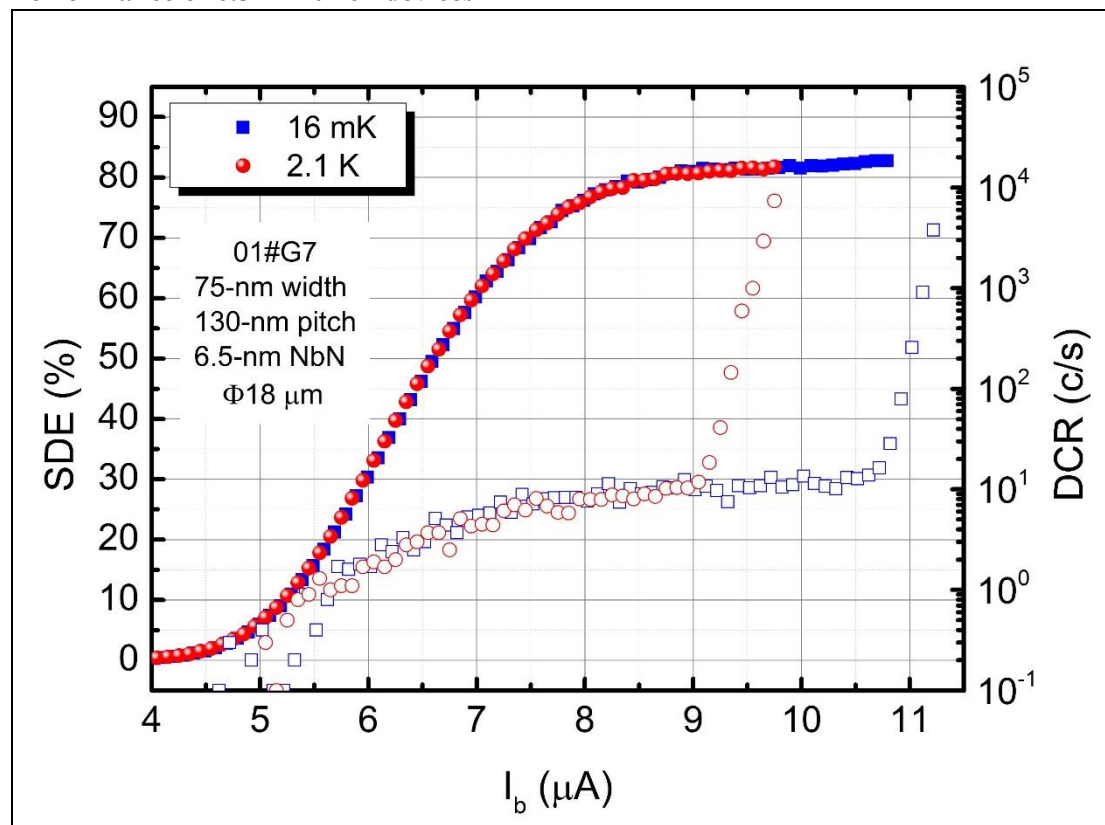
SDE and DCR performance of SNSPD 02#F9 cooled by a G-M cryocooler



Supplementary Figure 6. SDE and DCR vs. I_b for device 02#F9 measured using 2.13K G-M cryocooler. The SDE of 90.1% was obtained at a DCR of 10 Hz.

After the ultra-low temperature measurements, the device 02#F9 was mounted in a $2.125 \pm 0.005\text{K}$ G-M cryocooler. Supplementary Figure 6 demonstrated the SDE and DCR as functions of I_b . The measurement results are consistent with those measured in CDR operating at $2.10 \pm 0.06\text{K}$. The I_{sws} at CDR and G-M were 13.8 and $13.7 \mu\text{A}$ respectively, with a standard error about $0.05 \mu\text{A}$. The SDE of 90.1% was obtained at DCR of 10 Hz using G-M cryocooler.

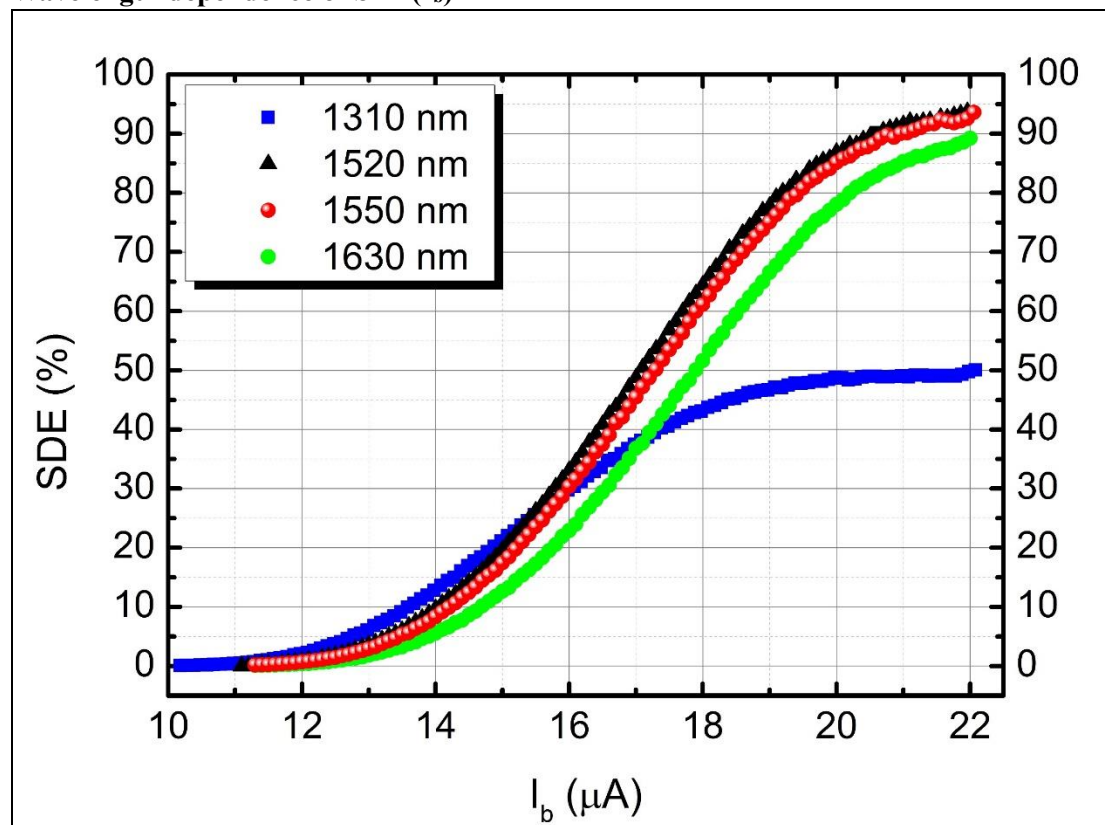
Performance of 6.5-nm-thick devices



Supplementary Figure 7. (Color online) Parallel polarized SDE and DCR vs. I_b for the device 01#G7, with an NbN thickness of 6.5 nm, measured at 2.1 and 16mK. A clear saturation plateau can be still observed at 2.1K, due to the reduction of thickness.

Supplementary Figure 7 shows the parallel polarized SDE and DCR as functions of I_b for the device 01#G7, measured at 2.1 and 16mK. This device was featured with a nominal 6.5-nm thick, 75-nm wide and 130-nm-pitch nanowire, covering an active area of $\Phi 18 \mu\text{m}$. Its I_{sw} of $11.2 \mu\text{A}$ at 16mK is lower than the ones described in Fig.2 (15.2 and $22.5 \mu\text{A}$) due to the thinner nanowire. Maximum SDE for this device was 82.2%, and the PER was 3.9 at 1550 nm. A significantly lower SDE was obtained in the thickness of 6.5 nm, than its simulated absorption of over 95%. This SDE was also about 10% lower than the 7(8)-nm-thick devices. We then carefully measured other devices in the same run and found the saturated SDEs was in the range of 70%-82%, varied by devices (Supplementary Table 1). Thus, the deviation between the experiment and simulation could be due to the thin nanowire combined with an imperfect DBR cavity, resulting in low photon absorption.

Wavelength dependence of SDE(I_b)

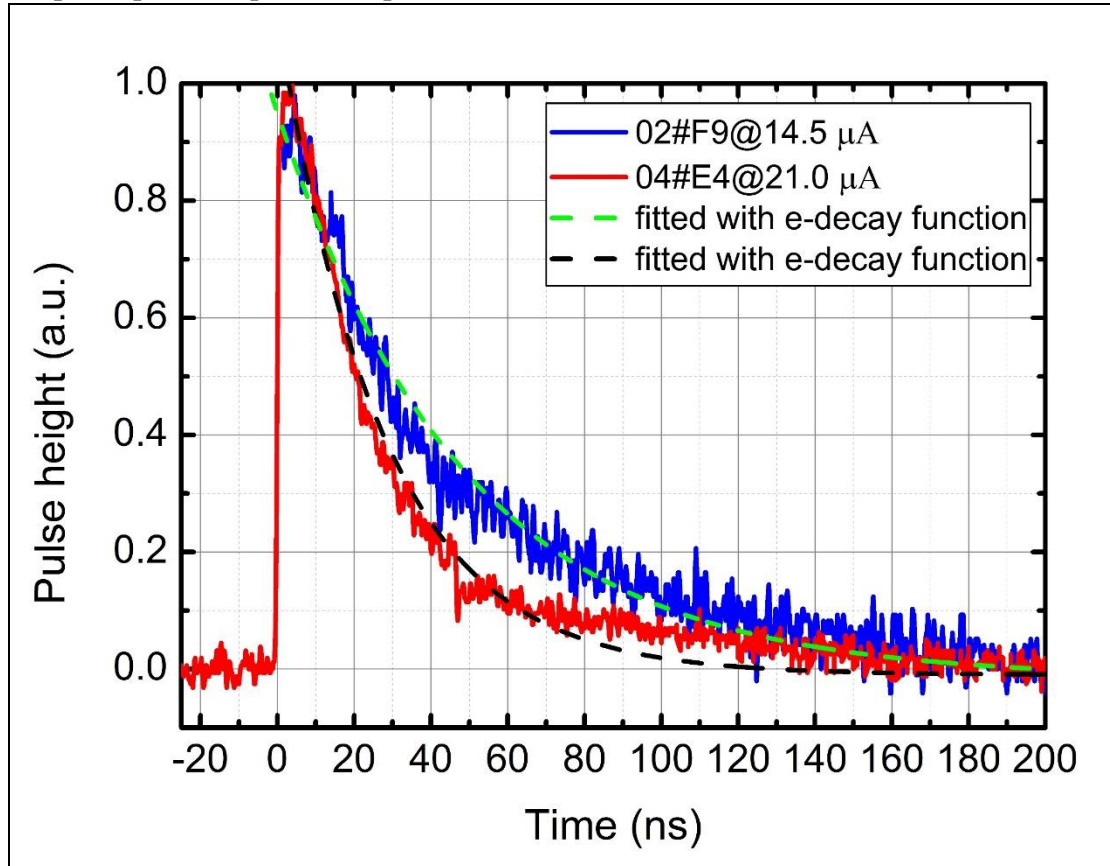


Supplementary Figure 8. (Color online) SDE vs. I_b for the device 04#E4, with various wavelength photons incidence, measured at 16mK. A clear saturation plateau was obtained at 1310 nm, due to the high excitation energy of 1310-nm photons.

In order to investigate the wavelength dependence of SDE, we illuminated the device with different wavelength photons. At each wavelength, the input photon power was carefully calibrated and attenuated to a flux of 5×10^4 photon/s. The photons at the wavelengths of 1520-1630 nm and 1310 nm were emitted from the CW-laser (Keysight 81940A), and ps-pulse-laser (Hamamatsu, C10196), respectively.

Supplementary Figure 8 shows the SDE as a function of I_b for device 04#E4, illuminated with 1310, 1520, 1550 and 1630 nm photons, measured at 16mK. At the wavelength of 1310 nm, a significant saturation can be obtained due the high excitation energy of 1310-nm photons. As the wavelength increased, the saturation plateau shrank and disappeared, indicated a non-unity IDE.

Response pulses of photon response



Supplementary Figure 9. (Color online) Response pulses of device 02#F9 and 04#F9 recorded by an oscilloscope at $I_b = 14.5$ and $21 \mu\text{A}$, respectively, when the devices operated at 16mK . The fast decay time of device 04#E4 was due to its small active area of $\Phi 15 \mu\text{m}$ and thick thickness.

We characterized the decay time of the response pulse by directly monitoring the amplified output electronic pulse with an oscilloscope. Response pulses of two devices 02#F9 and 04#F9 were shown in Supplementary Fig. 9, when the devices were biased at $I_b = 14.5$ and $21 \mu\text{A}$, respectively, and operated at 16mK . We fitted the decay time by using an exponential decay function expressed as $a + b \cdot (e^{-t/\tau})$, where τ is the time at which the height of the pulse is reduced to $1/e = 0.368$ to its initial value, a and b are fitting parameters. Thus, by the fitting the decay part of the pulse, we obtain the decay time $\tau = 48.5$ (27.3) ns for device 02#F9 (04#F9).

List of characterized devices

No.	Operating Temp. (K)	Thick. (nm)	W-P (nm)	Φ (μm)	I_{sw} (μA)	SDE_{max} (%)	PER	SDE_{ARC} (%)	PER_{ARC}
1	0.016	6.5	75-130	18	11.2	82.2	3.9	-	-
	2.1				10.0	81.4			
2	2.2	6.5	75-140	15	9.4	70.2	-	-	-
3	2.2	6.5	75-140	18	9.4	81.6	-	-	-
4	2.2	6.5	75-160	18	8.0	78.6	-	-	-
5	0.016	7.0	75-140	18	15.2	92.1	3.5	-	-
	2.1				13.8	90.2			
6	2.2	7.0	75-140	18	9.7	79.4	-	-	-
7	2.2	7.0	75-160	15	11.8	77.2	-	-	-
8	2.2	7.0	75-130	18	11.2	68.5	4.0	68.0	2.5
9	2.2	7.0	75-140	18	11.6	70.3	4.0	70.5	1.8
10	2.2	7.0	75-160	18	12.0	72.3	5.0	71.4	2.5
11	2.2	7.0	75-180	18	12.2	65.1	5.0	67.0	2.6
12	0.016	7.5	75-140	18	18.6	88.3	3.9	-	-
	2.1				17.6	87.0			
13	2.3	7.5	75-160	18	16.2	72.7	-	-	-
14	0.016	8.0	75-140	15	22.5	91.7	3.2	-	-
	2.1				20.4	76.5			
15	2.2	8.0	75-140	15	19.2	81.2	-	-	-
16	2.3	8.0	75-140	18	20.0	70.4	-	-	-

Supplementary Table 1 (Color online) List of characterized devices. From left to right: sequence numbers (No.), nanowire width (w) and pitch (p); diameter of active area (Φ), switching current (I_{sw}), maximal SDE (SDE_{max}), polarization extinction rate (PER). SDE_{ARC} : maximal SDE after anti-reflection coating (ARC). PER_{ARC} : PER measured after ARC. For the devices (No.8-11), the influence of the ARC were studied. The ARC layer was deposited by electron beam evaporation, with a SiO thickness of ~ 408 nm (i.e., $\lambda/2/n_{\text{SiO}}$, where $n_{\text{SiO}} = 1.89$ and λ is the target wavelength). The value of PER significant decreased after the ARC,

while the SDE did not showed a notable change.

Comparison of the designs and performances between NbN, MoSi, WSi-SNSPDs and W- TES

SNSPD				TES	
Material	Nb(Ti)N		MoSi ¹	WSi ²	W ³
Cavity design	half-cavity with DBR	double-side cavity	full-cavity with backside Au (Al for TES) mirror		
SDE (%) ~1550 nm	92.1@1.8K 90.2@2.1K	80@2.1K ⁴ 76@2.5K ⁵	87.1@0.7K 82@2.3K	93@0.12K 90@2K	95@0.1K
DCR (c/s)	10	1000	100	1000	N/A
Jitter (ps)	79@2.1K	40-80	99	150@0.12K	50000– 100000
I_{sw} (μA)	14.5@1.8K 13.8@2.1K	12@2.1K ⁴ 6.5@2.5K ⁵	9.5@0.7K 4.3@2.3K	4@0.12K 1.8@2k	~17@0.1K
Decaytime (ns)	48.5	5 ⁵ , ~30 ⁴	35	120 (rest time ~40 ns)	800
Package	fiber front-side package	fiber back-side package ⁴ ; nano-positioner ⁵	front-side fiber self-alignment package		

Supplementary Table 2 (Color online) Performance of the Nb(Ti)N, WSi, MoSi-SNSPDs and W-
TES at 1550 nm wavelength.

Supplementary References

1. Verma VB, *et al.* High-efficiency superconducting nanowire single-photon detectors fabricated from MoSi thin-films. *Optics express* **23**, 33792-33801 (2015).
2. Marsili F, *et al.* Detecting single infrared photons with 93% system efficiency. *Nat Photon* **7**, 210-214 (2013).
3. Lita AE, Miller AJ, Nam SW. Counting near-infrared single-photons with 95% efficiency. *Optics express* **16**, 3032-3040 (2008).
4. Yamashita T, Miki S, Terai H, Wang Z. Low-filling-factor superconducting single photon detector with high system detection efficiency. *Opt Express* **21**, 27177-27184 (2013).
5. Rosenberg D, Kerman AJ, Molnar RJ, Dauler EA. High-speed and high-efficiency superconducting nanowire single photon detector array. *Opt Express* **21**, 1440 (2013).